Thermodynamics and static response of anomalous one-dimensional fermions via a quantum Monte Carlo approach in the worldline representation

J. R. McKenney, A. Jose, and J. E. Drut
Department of Physics and Astronomy, University of North Carolina, Chapel Hill, North Carolina 27599, USA

(Received 9 March 2020; revised 23 July 2020; accepted 29 July 2020; published 14 August 2020)

A system of three-species fermions in one spatial dimension (1D) with a contact three-body interaction is known to display a scale anomaly. This anomaly is identical to that of a two-dimensional (2D) system of two-species fermions. The exact relation between those two systems, however, is limited to the two-particle sector of the 2D case and the three-particle sector of the 1D case. Here, we implement a nonperturbative Monte Carlo approach, based on the worldline representation, to calculate the thermodynamics and static response of three-species fermions in 1D, thus tackling the many-body sector of the problem. We determine the energy, density, and pressure equations of state and the compressibility and magnetic susceptibility for a wide range of temperatures and coupling strengths. We compare our results with the third-order virial expansion and interpret the classical-quantum crossover as the onset of trimer degrees of freedom.

DOI: 10.1103/PhysRevA.102.023313

I. INTRODUCTION

Recently, a series of papers [1–11] showed that fine-tuned one-dimensional (1D) systems (bosonic or fermionic) with *only three-body interactions* display anomalous scale invariance, and the researchers began studying many of the ensuing properties. These systems are classically invariant under scale transformations as they possess no intrinsic scale, but their quantum-mechanical version requires the introduction of a new scale, namely a regulator. The appearance of such a scale, often called dimensional transmutation, is well understood and has been described by many authors and in a variety of situations (see, e.g., Refs. [12–17]). In particular, the anomaly manifests itself as a correction to thermodynamic relations [18] and breathing modes [14,19,20] and also appears in the right-hand side of sum rules [19], where it is naturally related to the Tan contact [21–23].

In nonrelativistic physics, the paradigmatic example of a system with anomalous scale invariance is the two-dimensional (2D) Fermi gas with attractive two-body interactions. In recent years, that system has been vigorously studied both experimentally with ultracold atoms [24–34] and theoretically [14,19,20,35–38] (see Ref. [39] for a review). In contrast, studies of the 1D counterpart that we focus on here are still in their infancy. Furthermore, as shown in Ref. [5], these are the only two homogeneous systems with pure contact interactions (i.e., not involving derivatives) featuring anomalous scale invariance. Therefore, the question of whether the 1D system can be experimentally realized and studied is therefore of great interest, as is the issue of to what extent its behavior is in any way related to its 2D cousin. The two systems, despite their different spatial dimensionality, are actually related in a well-defined way: Ref. [5] found that the 1D three-body dynamics with a three-body interaction is identical to that of two particles in 2D with a two-body interaction (once the center-of-mass motion is factored out in both cases). From that property, the same work derived a cross-dimensional connection between virial coefficients. To that extent, the high-temperature behavior of these 1D and 2D systems is therefore equivalent.

The above cross-dimensional correspondence, however, appears to be limited to the three-body sector in 1D and the two-body sector in 2D. Beyond that point, the 1D system is not obviously related to the 2D system and should therefore be studied independently. Here, we contribute to those investigations by tackling a system of many fermions with a contact three-body interaction in a fully nonperturbative calculation of its thermodynamics and static response. To that end, we use a lattice formulation (i.e., we discretize space-time) and the worm algorithm form of quantum Monte Carlo (see below as well as Secs. II and III and Appendix B), and we explore a wide range of couplings and temperatures, furnishing predictions for future experiments. Where possible, we compare with the third-order virial expansion, using the equivalence between virial coefficients mentioned above.

The quantum Monte Carlo technique we use is essential toward obtaining the many-body properties. While powerful numerical (e.g., density-matrix renormalization group [40]) and analytic (such as bosonization, see, e.g., Ref. [41]) approaches have had immense success in 1D, the three-body interactions dramatically limit the available techniques. In particular, exact approaches such as the Bethe ansatz [42] are simply not applicable here. The formulation and algorithm we use follow closely those of Ref. [43] (see also Ref. [44]) and can be easily generalized to include two-body as well as four-body forces and beyond (such as those originally proposed in Ref. [45] and studied in detail in Refs. [46,47]), without suffering from a sign problem (in 1D). This indicates that a vast number of systems are open for research with the methods used and explained here. Furthermore, the experimental realization of

multiflavor systems with many-body forces is currently under intense investigation [4,10,48,49].

The remaining sections are organized as follows. In Sec. I we present the Hamiltonian, lattice theory, and the worldline representation, and we explain how the theory is renormalized. In Sec. II we describe in detail how the worldline representation is used to carry out Monte Carlo calculations of thermodynamic observables. Section III discusses our results for the various equations of state (density, energy, pressure, and Tan contact) as well as the compressibility and magnetic susceptibility. Finally, in Sec. IV we summarize and present our conclusions. Further technical details and cross-checks are given in Appendixes A–C.

II. HAMILTONIAN, LATTICE THEORY, AND MANY-BODY FORMALISM

We study a system of three-species fermions in 1D governed by the following Hamiltonian:

$$\hat{H} = \hat{T} + \hat{V}, \tag{1}$$

where the kinetic energy operator is $\hat{T} = \hat{T}_1 + \hat{T}_2 + \hat{T}_3$, where

$$\hat{T}_s = \int dp\, \frac{p^2}{2m} \hat{a}_s^\dagger(p)\hat{a}_s(p), \tag{2}$$

and the interaction energy operator is

$$\hat{V} = g \int dx\, \hat{n}_1(x)\hat{n}_2(x)\hat{n}_3(x). \tag{3}$$

Here, $\hat{a}_s^\dagger(p)$ and $\hat{a}_s(p)$ are the fermionic creation and annihilation operators for particles of species s and momentum p, and $\hat{n}_s(x)$ is the corresponding density at position x. From this point on, we take $m = \hbar = k_B = 1$.

To calculate the thermodynamics of this system, in particular the static response in the spin and density channels, we discretize space-time and use a nonperturbative Monte Carlo method, as explained next. Our starting point is the grand-canonical partition function

$$\mathcal{Z} = \mathrm{Tr}\big[e^{-\beta(\hat{H}-\mu\hat{N})}\big], \tag{4}$$

where the trace is over the Fock space, $\hat{H}$ is as in Eq. (1), $\hat{N} = \hat{N}_1 + \hat{N}_2 + \hat{N}_3$ is the total particle number operator, and $\hat{N}_i$ is the particle number operator for the ith species. We focus on unpolarized systems in this work, such that the chemical potential μ is the same for all species.

To address the Boltzmann operator when both $\hat{T}$ and $\hat{V}$ are present, taking into account that those operators do not commute, we implement the following steps. First, we place the system in a spatial lattice and choose a nearest-neighbor discretization of the kinetic energy, namely

$$\hat{T}_s = -\frac{1}{2}\sum_{i,j} \hat{\psi}_{s,i}^\dagger(\delta_{i,j+1} + \delta_{i,j-1} - 2\delta_{i,j})\hat{\psi}_{s,j}, \tag{5}$$

where $\hat{\psi}_{s,i}^\dagger$ and $\hat{\psi}_{s,i}$ respectively create and annihilate a fermion of species s at location i on the lattice.

Second, we write the on-site interaction as

$$\hat{V} = g\sum_i \hat{n}_{1,i}\hat{n}_{2,i}\hat{n}_{3,i}, \tag{6}$$

where $\hat{n}_{s,i} = \hat{\psi}_{s,i}^\dagger\hat{\psi}_{s,i}$, and the total particle number is therefore $\hat{N} = \hat{N}_1 + \hat{N}_2 + \hat{N}_3$, where

$$\hat{N}_s = \sum_i \hat{n}_{s,i}. \tag{7}$$

Using the above discretized forms (note that we have taken the spatial lattice spacing to be $\ell = 1$, but we retain τ as the imaginary-time lattice spacing), we may separate $\hat{H} - \mu\hat{N}$ into diagonal (or "on-site") and off-diagonal (or "hopping") pieces, respectively, $\hat{D}$ and $\hat{K}$:

$$\hat{H} - \mu\hat{N} = \hat{D} + \hat{K}, \tag{8}$$

where

$$\hat{D} = \sum_i (1-\mu)(\hat{n}_{1,i} + \hat{n}_{2,i} + \hat{n}_{3,i}) + g\hat{n}_{1,i}\hat{n}_{2,i}\hat{n}_{3,i}, \tag{9}$$

and $\hat{K} = \hat{K}_1 + \hat{K}_2 + \hat{K}_3$, where

$$\hat{K}_s = -\frac{1}{2}\sum_{i,j} \hat{\psi}_{s,i}^\dagger(\delta_{i,j+1} + \delta_{i,j-1})\hat{\psi}_{s,j}. \tag{10}$$

Armed with $\hat{D}$ and $\hat{K}$ as above, we proceed by implementing a Suzuki-Trotter decomposition:

$$e^{-\beta(\hat{H}-\mu\hat{N})} \simeq e^{-\tau\hat{K}}e^{-\tau\hat{D}}\cdots e^{-\tau\hat{K}}e^{-\tau\hat{D}} + O(\beta^2/N_\tau), \tag{11}$$

where N_τ factors are present on the right-hand side, such that $\beta = \tau N_\tau$. The above decomposition can be expressed as a hopping-parameter expansion (see Appendix A),

$$e^{-\beta(\hat{H}-\mu\hat{N})} \simeq e^{-\beta\hat{D}}\sum_{m=1}^{\infty}\sum_{k_m=1}^{N_\tau}\sum_{k_{m-1}=1}^{k_m-1}\cdots\sum_{k_1=1}^{k_2-1} e^{\tau k_m\hat{D}}(-\tau\hat{K})e^{-\tau k_m\hat{D}} \times\cdots\times e^{\tau k_1\hat{D}}(-\tau\hat{K})e^{-\tau k_1\hat{D}}. \tag{12}$$

The grand-canonical partition function corresponds to the trace of the above operator. Using a coordinate-space basis for all the operators involved, the trace can be written as a sum over configurations represented by lines, so-called worldlines, connecting the lattice points (see the description of the algorithm below). Each worldline represents how a given string of matrix products in Eq. (12) modifies a given basis wave function as it propagates in imaginary time. The worldlines are straight along the time direction unless an off-diagonal contribution $(-\tau\hat{K})$ appears, in which case a worldline will deform sideways at that particular time slice. Because a trace is involved, all worldlines begin and end at the same spatial point when traversing the full extent $\beta = \tau N_\tau$ of the time direction.

More specifically, the $\hat{K}_s$ factors are single-particle operators acting on each species independently, e.g.,

$$\langle X|\,(-\tau\hat{K}_1)\,|Y\rangle = \frac{\tau}{2}\big(\delta_{x_1,y_1+1} + \delta_{x_1,y_1-1}\big)\delta_{x_2,y_2}\delta_{x_3,y_3}, \tag{13}$$

where we have used $|Y\rangle = |y_1\rangle\,|y_2\rangle\,|y_3\rangle$, and similarly for $\langle X|$. The kinetic energy operator will allow a worldline to move sideways between two neighboring spatial points on a given time slice.

The diagonal piece, on the other hand, is a combination of one- and three-body operators and must therefore be treated

differently. To that end, we write

$$e^{-\tau\hat{D}} = \prod_i e^{-\tau k\hat{n}_{1,i}} e^{-\tau k\hat{n}_{2,i}} e^{-\tau k\hat{n}_{3,i}} e^{-\tau g\hat{n}_{1,i}\hat{n}_{2,i}\hat{n}_{3,i}}, \quad (14)$$

where $k = 1 - \mu$, and moreover we note that

$$e^{-\tau k\hat{n}_{s,i}} = 1 + (e^{-\tau k} - 1)\hat{n}_{s,i}, \quad (15)$$

which is diagonal in coordinate space and always equal to $e^{-\tau k} = e^{\tau(\mu-1)}$, and

$$e^{-\tau g\hat{n}_{1,i}\hat{n}_{2,i}\hat{n}_{3,i}} = 1 + (e^{-\tau g} - 1)\hat{n}_{1,i}\hat{n}_{2,i}\hat{n}_{3,i}. \quad (16)$$

which is also diagonal and always equal to 1 unless the initial and final states contain three nonidentical particles that share the same location, in which case the interaction operates too and the matrix element equals $e^{-\tau g}$. When the worldlines of all three flavors coincide at a given point in space and time, the interaction will operate and yield a nontrivial contribution to that particular term.

Renormalization

As the Hamiltonian (1) features an ultraviolet divergence in 1D, the coupling g must be renormalized [5]. In this work, however, as we employ open boundary conditions to avoid the infamous sign problem; the renormalization condition of Ref. [5] is inapplicable. Instead, we numerically solve the three-body problem at each coupling strength along the lines of the iterative method presented in Ref. [6]. In particular, after expanding in a sine-wave basis, the value of the wave function for wave numbers n, m, l is

$$\phi_{nml} = -\frac{8g/L^3}{\epsilon_{nml} + \epsilon_B} \sum_{i,j,k} \phi_{ijk} S^{ijk}_{nml}, \quad (17)$$

where the lattice length $L = N_x + 1$, the kinetic energy is $\epsilon_{nml} = \epsilon_n + \epsilon_m + \epsilon_l - 3\epsilon_1$, and the effective binding energy is $\epsilon_B = -(E - 3\epsilon_1)$. (Here, $\epsilon_k = 1 - \cos(k\pi/L)$, and the ground-state kinetic energy $3\epsilon_1$ is subtracted to ensure $\epsilon_B \geqslant 0$.) The factor S^{ijk}_{nml} is given by the overlap of the six sine-wave basis functions corresponding to its upper and lower indices as wave numbers:

$$S^{ijk}_{nml} = \sum_{x=1}^{N_x} \prod_q \sin\left(\frac{q\pi}{L}x\right), \quad (18)$$

where $q \in \{i, j, k, n, m, l\}$. For given values of ϵ_B and L, the value of g which solves Eq. (17) for all n, m, l is the renormalized coupling. The resulting relationship between g and $\beta\epsilon_B$ is shown in Fig. 1. As expected, the dependence shows logarithmic behavior $-g^{-1} \propto \ln(\beta\epsilon_B)$, for large enough $\beta\epsilon_B$.

As a final consideration of the lattice method, we now address dimensionless parameters and finite-size effects. To approach both the continuum and the thermodynamic limits, we must satisfy the separation of scales

$$\ell \ll \lambda_T, \ \lambda_F \ll L, \quad (19)$$

where the thermal wavelength $\lambda_T = \sqrt{2\pi\beta}$, $\lambda_F = n^{-1}$ is the interparticle distance, $n = N/L$ is the total density, and $\ell = 1$. For fixed $\beta\mu$ and λ_T/L, a given value of $\beta\epsilon_B$ fixes the physical coupling strength. Given a value $\lambda_T/L \ll 1$, we increase β and L until achieving numerical convergence in the observables, at fixed $\beta\mu$ and $\beta\epsilon_B$. We performed multiple calculations in which we varied those last two parameters (i.e., in all of the plots below, each point corresponds to a different Monte Carlo calculation). By varying $\beta\mu$ at fixed $\beta\epsilon_B$, we explore different density regimes at fixed coupling strength. As we place our system on a lattice, large $\beta\mu$ eventually yields high densities, such that the condition $\ell \ll \lambda_F$ is not satisfied and lattice effects appear (i.e., we depart from the continuum limit; we return to this issue below).

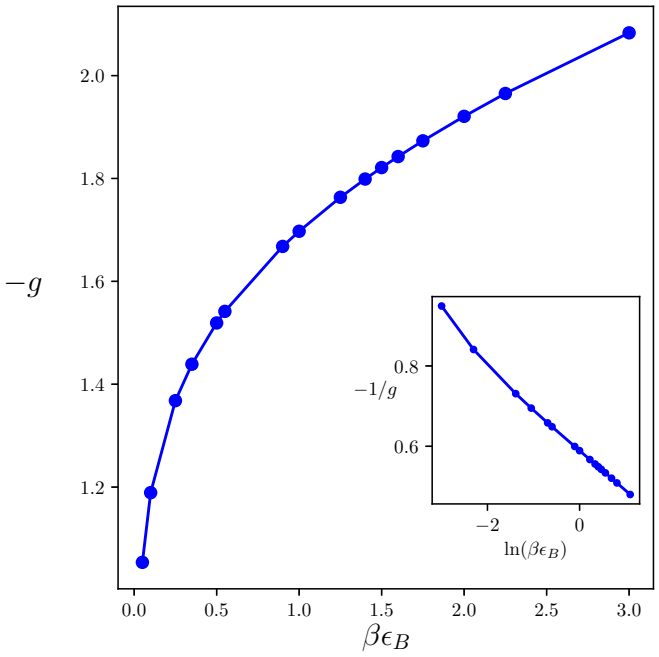

FIG. 1. The dimensionless coupling g as a function of the binding energy ϵ_B in the dimensionless combination $\beta\epsilon_B$ for $N_x = 80$. Inset: $-g$ as a function of $\ln(\beta\epsilon_B)$.

III. UPDATE ALGORITHM AND MEASUREMENT OF OBSERVABLES

To carry out the Monte Carlo sampling of the partition function in the worldline representation [Eqs. (4) and (12)], we employ the "worm" algorithm as described in Ref. [43], adapting it to the case of three fermion species with a three-body interaction.

The worm algorithm evolves the system from one configuration c of a set of worldlines (Fig. 2) to another by a series of contiguous local updates. The path traversed through the space-time lattice by this series of updates is known as the "worm"; each individual local update occurs at the location of the "head" of the worm. At the beginning of each update, a space-time lattice site is chosen at random; this site becomes the "tail" of the worm. The head departs from the tail, effecting local updates as it meanders through the lattice. The update is complete when the head reunites with the tail, thereby closing a completed worldline or else annihilating a previously existing one.

At each site visited by the head, the local update must obey detailed balance. As transition probabilities that satisfy this requirement are tabulated in Ref. [43], we do not reproduce

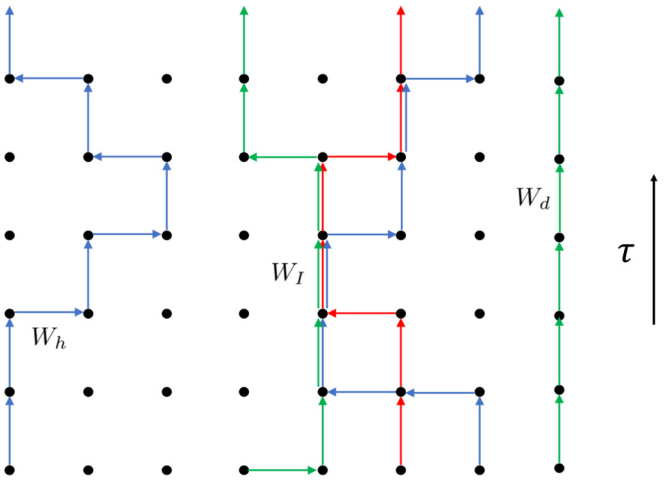

FIG. 2. Example configuration of worldlines contributing to Eq. (12), where the three different colors correspond to the three fermionic species. Instances of the different weights are labeled where they occur; note that all worldlines are periodic in the temporal direction.

them here; we do, however, note that the relevant weights appear as

$$W_d = e^{\tau(\mu-1)}, \tag{20}$$

$$W_h = \tau/2, \tag{21}$$

$$W_I = e^{-\tau g}, \tag{22}$$

where W_d corresponds to the diagonal term $\hat{D}$, W_h to the hopping term $\hat{K}$, and W_I to the interacting contribution that occurs when three worldlines of different flavors share a timelike bond (wherever W_I occurs, the three diagonal contributions $(W_d)^3$ are present as well). Instances of each of these weights are illustrated in Fig. 2. For completeness, we provide a map of all possible[1] local updates in Appendix B.

In terms of the weights listed above, the total weight of a space-time lattice configuration c is [43]

$$\Omega(c) = (W_d)^{N_\tau N}(W_h)^{n_h}(W_I)^{n_I}, \tag{23}$$

where n_h is the total number of hops among all fermion species, and n_I is the number of interacting timelike bonds ($n_I = 1$ in Fig. 2). Now, the partition sum may be written as

$$\mathcal{Z} = \sum_c \Omega(c), \tag{24}$$

so that observables, generally given by

$$\langle \hat{O} \rangle = \frac{1}{\mathcal{Z}} \sum_c O(c)\,\Omega(c), \tag{25}$$

may be computed by taking suitable log-derivatives of Eq. (24). As an example, the energy of a single configuration

[1]Sites on the spatial boundaries have restricted sets of transitions, and the associated probabilities are modified; these are excluded from Appendix B due to their negligible contribution in the large-volume limit.

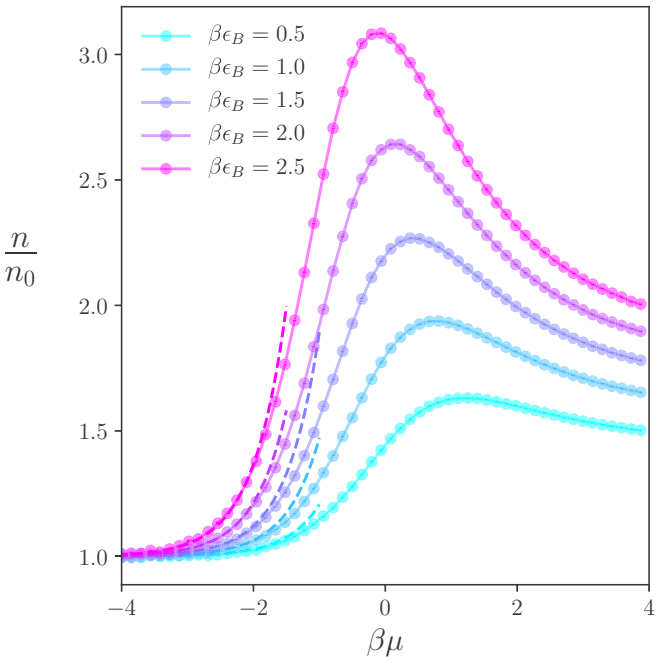

FIG. 3. The density n in units of the noninteracting density n_0 as a function of the dimensionless parameter $\beta\mu$ and the coupling strength $\beta\epsilon_B$ (increasing coupling from bottom curve to top curve). The solid lines interpolate the Monte Carlo results (shown with circles); the dashed lines show the third-order virial approximations.

c is calculated as

$$E(c) = N - \frac{n_h}{\beta} + g\frac{n_I}{N_\tau}. \tag{26}$$

With configurations generated by the worm algorithm, Eq. (25) is simply evaluated as the arithmetic mean of the observable's value over the sampled configurations (after allowing for decorrelation between consecutive samples).

IV. RESULTS

We carried out our Monte Carlo calculations in lattices of spatial size $N_x = 80$ and temporal size $N_\tau = 3600$, with corresponding lattice spacings $\ell = 1$ and $\tau = 0.005$, such that $L = (N_x + 1)\ell = 81$ (we used hard-wall boundary conditions in the spatial directions) and $\beta = N_\tau\tau = 18$. We obtained data for five unique couplings, corresponding to $\beta\epsilon_B = 0.5$, 1.0, 1.5, 2.0, and 2.5. At the time of sampling, the particle density and energy were recorded, taking a total of 2×10^5 decorrelated samples. The required decorrelation time was estimated by taking samples every 100 to 10 000 worm updates per fermion species and finding no noticeable differences in the results. Using these quantities and the appropriate Maxwell relations, we report other significant thermodynamic properties. Most values are reported as a ratio with respect to their noninteracting counterparts, as detailed below.

A. Equations of state: Density, energy, pressure, and contact

The top of Fig. 3 displays the interacting total density n in units of its noninteracting counterpart n_0, as a function of $\beta\mu$, for several coupling strengths. The solid line interpolates

the density for the values of $\beta\mu$ that were not explicitly calculated. For reference, we note that the total noninteracting density is derived from the Fermi-Dirac distribution,

$$n_0 = \frac{3}{L}\sum_{k=1}^{N_x} \frac{e^{-\beta(\epsilon_k-\mu)}}{1+e^{-\beta(\epsilon_k-\mu)}}, \tag{27}$$

where $\epsilon_k = 1-\cos(k\pi/L)$ is simply the Hubbard dispersion relation resulting from nearest-neighbor hopping (i.e., a double-difference formula for the second derivative). In the same figure, we compare our results to the third-order virial expansion

$$n\lambda_T/3 = z + 2b_2^0 z^2 + 3(b_3^0+\Delta b_3)z^3, \tag{28}$$

where $\lambda_T = \sqrt{2\pi\beta}$, $z = e^{\beta\mu}$ is the fugacity, and b_i^0 is the ith noninteracting virial coefficient. As shown in Ref. [5], Δb_3 is related to the second-order virial coefficient Δb_2^{2D} of 2D, two-species fermions by

$$\Delta b_3 = \frac{1}{\sqrt{3}}\Delta b_2^{2D}, \tag{29}$$

where

$$\Delta b_2^{2D}(\beta\epsilon_B) = \nu(\beta\epsilon_B) = \int_0^\infty dt\, \frac{(\beta\epsilon_B)^t}{\Gamma(t+1)}. \tag{30}$$

The density equation of state n/n_0 displays the same characteristic behavior observed in both 1D and 2D Fermi systems with two-body interactions [37,50]: a rapid healing to the virial expansion at negative $\beta\mu$; a maximum where quantum fluctuations dominate, typically around $\beta\mu = 0$; and a relatively mild decay at large and positive $\beta\mu$, where the increased density tends to partially quench interaction effects. The role of the interaction in that regime is largely reduced to trimer formation. The residual, repulsive trimer-trimer interaction is due to Pauli exclusion of the fermionic components.

In addition to the density, we calculated the energy equation of state across multiple chemical potentials and couplings, as shown in the bottom of Fig. 4. There, the energy $E = \langle\hat{H}\rangle$ is shown in units of its noninteracting value given by

$$E_0 = 3\sum_{k=1}^{N_x} \frac{\epsilon_k\, e^{-\beta(\epsilon_k-\mu)}}{1+e^{-\beta(\epsilon_k-\mu)}}. \tag{31}$$

The energy equation of state E/E_0 displays features with obvious counterparts in the density described above. Indeed, E/E_0 heals to the virial expansion at large negative $\beta\mu$; the interplay of quantum and interaction fluctuations results in a broad minimum around $\beta\mu = 0$ for all couplings; and finally, at large positive $\beta\mu$, the interaction effects are progressively softened.

The analysis of Refs. [5,6] suggested that this system undergoes a "Fermi-Fermi crossover" in moving from weak to strong coupling, where, starting from three species of ideal Fermi gases, increasing attraction causes the formation of a repulsive Fermi gas of composite trimers. In the limit of infinite coupling strength, we anticipate that as the trimer radius shrinks to zero, the repulsion between trimers will give way to ideal behavior, so that the trimers will behave as a hard-core Bose gas in 1D [51]. With our many-body results, we may shed additional light on this question.

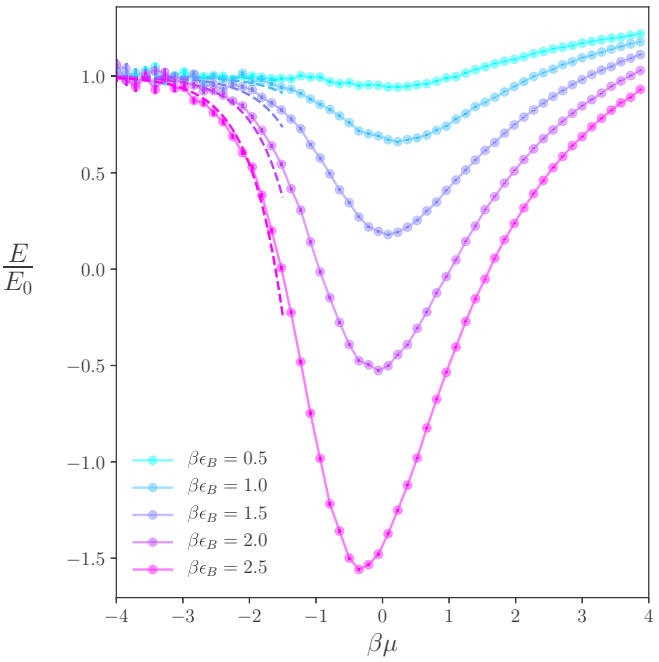

FIG. 4. The total energy E in units of the noninteracting energy E_0 as a function of the dimensionless parameter $\beta\mu$, for several values of the coupling $\beta\epsilon_B$ (same values as in Fig. 3, but increasing in coupling from the top curve to the bottom curve). The solid lines interpolate the Monte Carlo results (shown with circles); the dashed lines show the third-order virial approximations.

To compare our results with an ideal Fermi gas of trimers, we calculate the energy of the trimer gas E_{trimer} as follows. For a given value of β and μ, the trimer chemical potential μ_{trimer} is tuned so that the total number of particles is equal in both systems: $3N_{\text{trimer}} = N$. The trimer gas energy is then computed as $E_{\text{trimer}} = \langle E\rangle_{\text{trimer}} - \epsilon_B N/3$, where the expectation value is that of an ideal Fermi gas with mass $3m$. In Fig. 5, the difference in energy per particle $\mathcal{E} = E/N$ between our results and the ideal trimer gas is displayed, showing that increasing the coupling strength does indeed cause the system to approach the trimer gas. The positivity of each of the curves supports the prediction of Ref. [6] that, for finite coupling, the effective interaction between trimers is repulsive.

From the density equation of state, the pressure can be obtained by integration, namely

$$P\lambda_T^3 = 2\pi\int_{-\infty}^{\beta\mu} d(\beta\mu)' n\lambda_T. \tag{32}$$

For reference, we note that the noninteracting pressure is given by

$$P_0 = \frac{3}{\beta L}\sum_{k=1}^{N_x} \ln\left(1+e^{-\beta(\epsilon_k-\mu)}\right). \tag{33}$$

Our results using the above expressions and numerical integration are shown in Fig. 6. To carry out the integration, the virial expansion was used as a boundary condition at large negative $\beta\mu$; specifically, the virial approximation

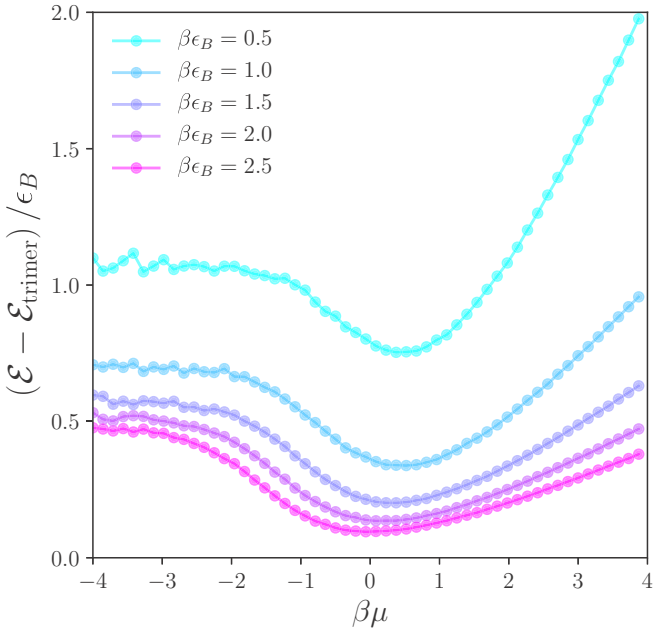

FIG. 5. Difference in energy per particle $\mathcal{E} = E/N$ (in units of ϵ_B) between the interacting system and the energy per particle $\mathcal{E}_{\rm trimer}$ of the corresponding ideal gas of composite trimers (with the same total particle number; see text), as a function of the dimensionless parameter $\beta\mu$. The dimensionless coupling strength $\beta\epsilon_B$ in each data set increases from top to bottom.

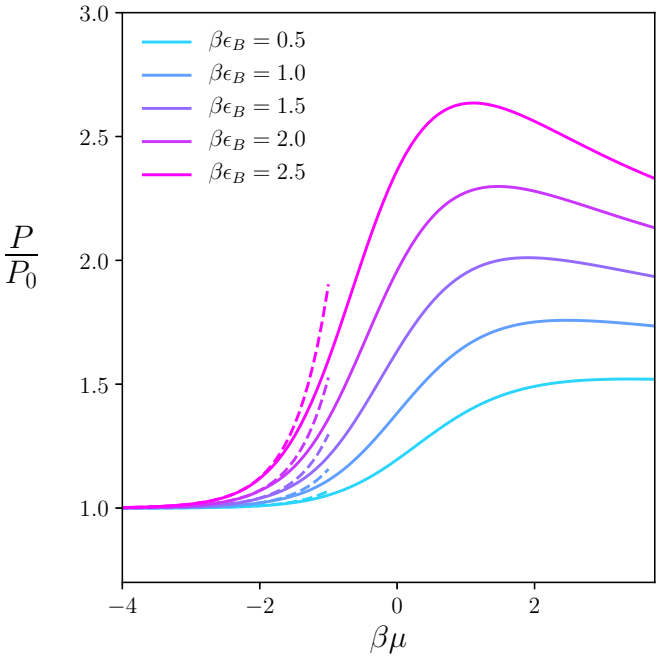

FIG. 6. The pressure P in units of the noninteracting pressure P_0 as a function of $\beta\mu$, obtained by numerical integration of the density equation of state. The dashed line is the result from the third-order virial approximation. The coupling strength $\beta\epsilon_B$ in each data set increases from bottom to top.

of Eq. (28) was used for $\beta\mu < -4$ in the integrand of Eq. (32). The interpretation of the behavior of the pressure is essentially the same as that of the density equation of state: as $\beta\mu$ is increased, the system traverses a crossover from the virial-expansion region to a quantum-dominated region where repulsive trimers dominate the picture. The main motivation for showing the pressure here is, therefore, simply to provide it for future reference, as it is often available from ultracold atom experiments.

Tan's contact density, which governs the behavior of correlation functions at short distances [21–23], can be calculated in our approach via

$$\mathcal{C} = \frac{2}{\beta L}\frac{\partial \ln \mathcal{Z}}{\partial \ln(\beta\epsilon_B)} = -2\frac{\langle \hat{V}\rangle}{L}\frac{\partial \ln g}{\partial \ln(\beta\epsilon_B)}, \tag{34}$$

where the $\langle \hat{V}\rangle$ factor encodes the many-body aspects of the problem, whereas $\partial \ln g/\partial \ln(\beta\epsilon_B)$ is fully determined by the renormalization of g, i.e., purely three-body physics.

In Fig. 7 we show our results for $\mathcal{C}$ as a function of $\beta\mu$ and for several values of the coupling strength. Also shown in the figure is the third-order virial expansion, given by

$$\mathcal{C} = \frac{2Q_1}{\beta L} z^3 \frac{1}{\sqrt{3}} \int_0^\infty dt\, \frac{t\,(\beta\epsilon_B)^t}{\Gamma(t+1)} + O(z^4), \tag{35}$$

where we have used Eq. (34) together with Eqs. (29) and (30) and the fact that, for our system,

$$\ln(\mathcal{Z}/\mathcal{Z}_0) = Q_1 \Delta b_3 z^3, \tag{36}$$

where $\mathcal{Z}_0$ is the noninteracting grand-canonical partition function and

$$Q_1 = 3\sum_k e^{-\beta\epsilon_k} \tag{37}$$

is the single-particle partition function.

The contact can also be obtained from the pressure-energy relation, which in 1D takes the form $P - 2E/L = \mathcal{C}$. However, the latter relies on nonrelativistic invariance, which is broken by lattice artifacts, and therefore yields somewhat different results at strong coupling or large densities (see Appendix C).

Finally, we note that, using the density equation of state shown above, one may connect our results as a function of $\beta\mu$ with the more conventional temperature scale T/ϵ_F, where $\epsilon_F = (n/3)^2$, as well as with the more conventional coupling scale ϵ_B/ϵ_F. To that end, we display in Fig. 8 the quantity T/ϵ_F as a function of ϵ_B/ϵ_F, for each value of $\beta\epsilon_B$ we studied. From this plot one sees, for instance, that at fixed ϵ_B/ϵ_F, increasing $\beta\epsilon_B$ yields lower temperature T/ϵ_F.

B. Static response functions: Compressibility and magnetic susceptibilities

As the three fermion species' chemical potentials may each be tuned independently, there are three independent magnetization (or polarization) parameters. By using scaled Jacobi coordinates, these parameters may be expressed in terms of previously defined quantities as follows. The first is

$$\hat{M}_1 = \hat{N} = \hat{N}_1 + \hat{N}_2 + \hat{N}_3 \tag{38}$$

and corresponds to the total particle number and thus reflects compressibility effects (see below), rather than polarization.

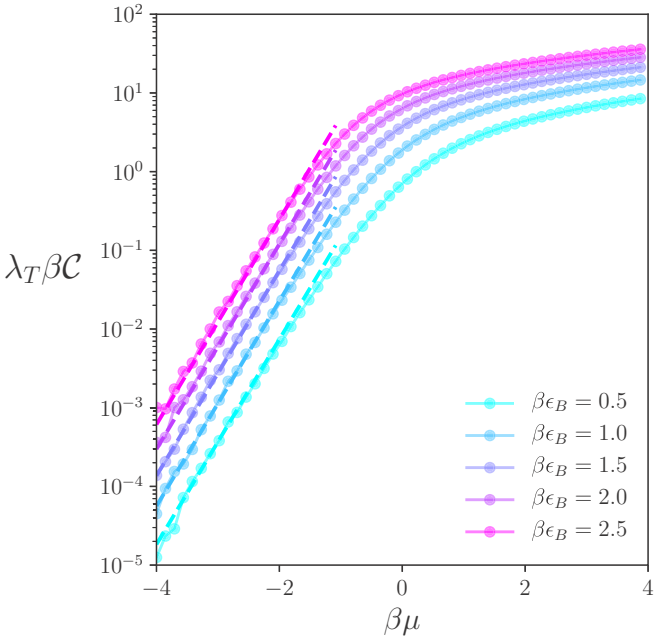

FIG. 7. Contact density $\mathcal{C}$ obtained from the expectation value of the potential energy, as a function of $\beta\mu$ and for several values of the coupling strength. The third-order virial expansion, shown with dashed lines, is seen to completely capture $\mathcal{C}$ for $\beta\mu < -1$. The coupling strength $\beta\epsilon_B$ in each data set increases from bottom to top.

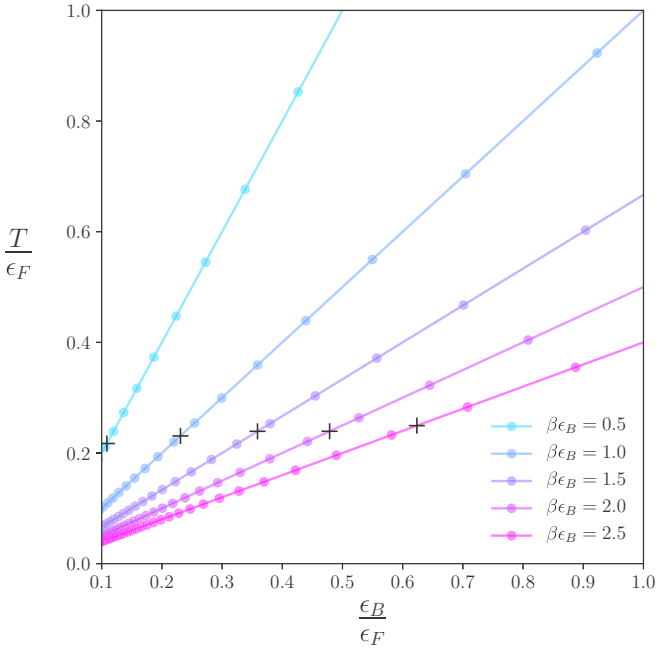

FIG. 8. The temperature scale T/ϵ_F as a function of the binding energy ϵ_B/ϵ_F, where $\epsilon_F = n^2$, for each of the couplings studied. The solid lines interpolate our Monte Carlo results shown in circles. The crosses mark the locations of the maxima in n/n_0 at the corresponding coupling strengths (see Fig. 3). The coupling strength $\beta\epsilon_B$ in each data set increases from top to bottom.

The other two capture differences in particle content among the three flavors and quantify the degree to which the system is polarized:

$$\hat{M}_2 = \tfrac{3}{2}(\hat{N}_1 - \hat{N}_2), \tag{39}$$

$$\hat{M}_3 = \tfrac{1}{2}(\hat{N}_1 + \hat{N}_2) - \hat{N}_3, \tag{40}$$

where overall factors are unimportant. The only requirement is that the applied fields h_i, defined in terms of the μ_i, leave invariant the inner product

$$\sum_i h_i \hat{M}_i = \sum_i \mu_i \hat{N}_i. \tag{41}$$

Thus, we have isothermal susceptibilities associated with each $\hat{M}_i$ and given by

$$\chi_i = \beta\left(\langle \hat{M}_i^2 \rangle - \langle \hat{M}_i^2 \rangle\right), \tag{42}$$

where the polarizations $\hat{M}_i$ may be expressed in terms of the particle numbers $\hat{N}_i$ as shown above.

For balanced systems where $\mu_1 = \mu_2 = \mu_3 = \mu$, so that $h_2 = h_3 = 0$, $h_1 = \mu$, χ_2 and χ_3 take on the same form when expressed in terms of their noninteracting counterparts:

$$\frac{\chi_2}{\chi_2^0} = \frac{\chi_3}{\chi_3^0} = \frac{\langle \hat{N}_i^2 \rangle - \langle \hat{N}_i \hat{N}_j \rangle}{\langle \hat{N}_k^2 \rangle_0 - \langle \hat{N}_k \hat{N}_l \rangle_0}, \tag{43}$$

where $i \neq j$, $k \neq l$, and $\langle \cdot \rangle_0$ denotes the noninteracting expectation value.

Note that, to determine the isothermal compressibility κ, we study the fluctuations in particle number:

$$\langle \hat{N}^2 \rangle - \langle \hat{N} \rangle^2 = \frac{1}{\beta}\left(\frac{\partial N}{\partial \mu}\right)_{T,V}, \tag{44}$$

such that

$$\kappa = \frac{L\beta\left(\langle \hat{M}_1^2 \rangle - \langle \hat{M}_1 \rangle^2\right)}{\langle \hat{M}_1 \rangle^2} = \frac{L\chi_1}{\langle \hat{M}_1 \rangle^2}. \tag{45}$$

In Fig. 9 we show κ/κ_0, where κ_0 is the compressibility of the noninteracting system, given by

$$\kappa_0 = \frac{3\beta}{4Ln_0^2} \sum_{k=1}^{N_x} \cosh^{-2}\left[\frac{\beta}{2}(\epsilon_k - \mu)\right], \tag{46}$$

with n_0 from Eq. (27). At large negative $\beta\mu$, the ratio κ/κ_0 approaches unity: in that region the response of the system is essentially that of a noninteracting system, with corrections given by the virial expansion (as shown previously for the density and the pressure equations of state). As $\beta\mu$ is increased away from the virial-expansion region, the response is increasingly that of a system of repulsively interacting trimers. Notably, that approach is not monotonic: as $\beta\mu$ is increased, κ/κ_0 first increases above unity before decreasing substantially as the classical-quantum crossover (the region around $\beta\mu \simeq 0$) is traversed, and then increasing again after that, reflecting the interplay between the attractive interaction and the trimer-trimer repulsion as the density is increased. The same type of behavior was found in both 1D and 2D Fermi systems with two-body interactions [37,50]. (The inset

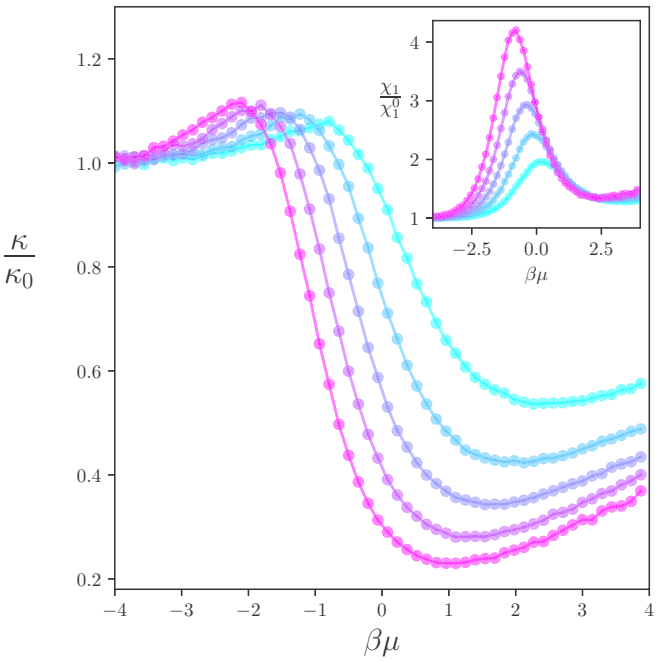

FIG. 9. Compressibility κ in units of its noninteracting value κ_0, as a function of $\beta\mu$, for several values of the coupling $\beta\epsilon_B$ (increasing from top to bottom on the right side of the plot). The solid lines interpolate our Monte Carlo results shown in circles. Inset: χ_1/χ_1^0 as a function of $\beta\mu$, representing the variance of the total particle number. The inset coupling strength increases from bottom to top (reverse order as in the main plot).

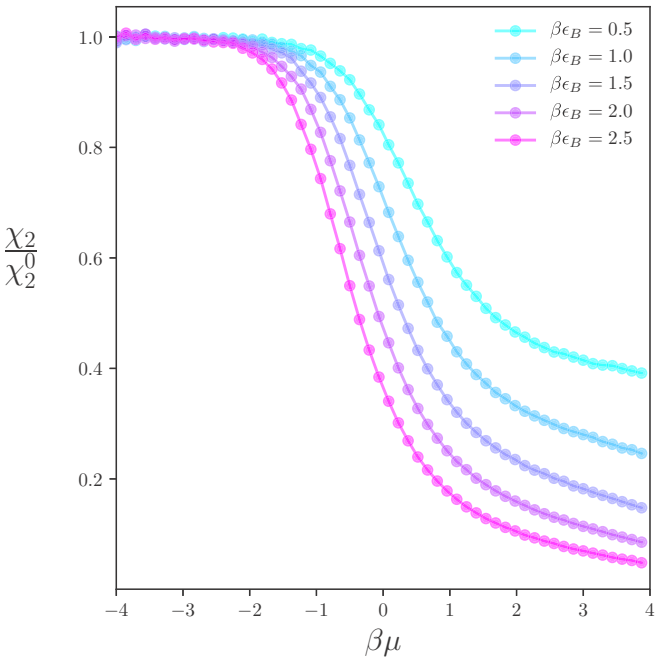

FIG. 10. The interacting susceptibility χ_2, in units of its noninteracting counterpart χ_2^0, as a function of $\beta\mu$. The solid lines interpolate our Monte Carlo results shown in circles. The coupling strength $\beta\epsilon_B$ in each data set increases from top to bottom.

of Fig. 9 shows more explicitly how interaction effects on the density fluctuations attain a broad maximum as $\beta\mu = 0$ is approached from the left and decay to a constant after that.)

In Fig. 10 we show the magnetic susceptibility χ_2/χ_2^0, per Eq. (43), i.e., showing the ratio of the interacting and noninteracting particle-number variances. At large negative $\beta\mu$, the ratio approaches unity, such that the response of the system to a chemical potential imbalance among species is essentially that of a noninteracting system, regardless of the coupling strength. On the other hand, as the density or the coupling grow, the susceptibility becomes increasingly governed by trimers and is therefore monotonnically more suppressed as a function of $\beta\mu$. Not unexpectedly, this is markedly different from the compressibility, as both interactions favor trimer formation.

V. SUMMARY AND CONCLUSIONS

In this work we have implemented a nonperturbative stochastic method to investigate the properties of nonrelativistic fermions in 1D with attractive three-body interactions. As previous works have noted, this system displays a scale anomaly: it is classically scale invariant in the sense that the coupling constant is dimensionless, but quantum fluctuations generate a three-body bound state and thus scale invariance is broken. There is, furthermore, an exact correspondence between the three-body sector of this system and the two-body sector of the analog system in 2D with two-body interactions. However, that correspondence is limited to those specific sectors and does not extend to higher particle numbers or thermodynamics (certainly not easily). Therefore, here we set out to provide a first characterization of the thermodynamics.

Using the worldline representation of the partition function, and using hard-wall boundary conditions, the sign problem can be completely avoided in this 1D system, even though the number of species is odd. With that approach, supplemented by the worm algorithm, we have calculated several equations of state: density, energy, and pressure, as well as Tan's contact. Additionally, we have characterized the static thermodynamic response by calculating the compressibility and the magnetic susceptibility. Our findings support the notion of a continuous Fermi-Fermi crossover, originally pointed out and explored in Refs. [5,6], whereby a trimer gas with repulsive interactions is approached at low temperatures, high-densities, or strong couplings.

As with similar systems with short-range interactions in 1D [50] and 2D [37], the interaction effects on the compressibility are maximized in the vicinity of $\beta\mu = 0$. Indeed, at large negative $\beta\mu$, the system is very dilute and governed by few-particle physics (i.e., the virial expansion), where kinetic energy contributions typically dominate; on the other hand, at large positive $\beta\mu$, the compressibility should approach that of a system of (fermionic) trimers with repulsive interactions. Notably, that approach is not monotonic: as $\beta\mu$ is increased, κ/κ_0 first increases above unity before decreasing substantially as the classical-quantum crossover (the region around $\beta\mu \simeq 0$) is traversed, and then increasing again after that. On the other hand, the magnetic susceptibility is monotonically suppressed as $\beta\mu$ or the coupling strength are increased, as trimer binding dominates that response function.

As mentioned in the Introduction, using the same technique it is possible to study this same system at finite chemical potential imbalance as well as with an increasing number of fermion species. This could be an interesting avenue for research in connection with the study of droplet formation and stability in these systems [1,2]. Notably, the same algorithm, with minor modifications, can be used to study systems with not only three-body forces but also two- and four-body forces (such as those originally proposed in Ref. [45] and studied in detail in Refs. [46,47]), as well as their generalization to multispecies cases mentioned above. All of the above can be carried out without a sign problem, as long as one remains in 1D with hard-wall boundary conditions and with the nearest-neighbor kinetic-energy discretization used here. We leave such studies for future work.

ACKNOWLEDGMENTS

We thank H. Singh and S. Chandrasekharan for helpful discussions and comments on the manuscript. This work was supported by the U.S. National Science Foundation under Grant No. PHY1452635.

APPENDIX A: HOPPING-PARAMETER EXPANSION

In this Appendix we derive the hopping-parameter expansion of Eq. (12) by two methods: starting from a lattice formulation, and starting from a continuum formulation (and discretizing at the end).

For the first approach, starting from the Suzuki-Trotter decomposition

$$e^{-\beta(\hat{H}-\mu\hat{N})} \simeq e^{-\tau\hat{K}}e^{-\tau\hat{D}}\ldots e^{-\tau\hat{K}}e^{-\tau\hat{D}} + O(\beta^2/N_\tau), \quad \text{(A1)}$$

with $\beta = \tau N_\tau$, we proceed by expanding the $e^{-\tau\hat{K}}$ factors in a power series:

$$e^{-\beta(\hat{H}-\mu\hat{N})} \simeq \sum_{k_j=0}^{\infty} \frac{(-\tau\hat{K})^{k_{N_\tau}}}{k_{N_\tau}!} e^{-\tau\hat{D}} \ldots \frac{(-\tau\hat{K})^{k_1}}{k_1!} e^{-\tau\hat{D}}. \quad \text{(A2)}$$

We then organize the above multiple sum according to the value of $n = \sum_j k_j$. The $n = 0$ order simply yields $e^{-\beta\hat{D}}$. For $n = 1$ we obtain

$$e^{-\beta\hat{D}} \sum_{k_1=1}^{N_\tau} e^{\tau k_1\hat{D}}(-\tau\hat{K})e^{-\tau k_1\hat{D}}. \quad \text{(A3)}$$

For $n = 2$ we have two kinds of contributions: those which apply $\hat{K}$ twice at the same time slice (N_τ terms, each with an extra factor of $1/2!$); and those which apply $\hat{K}$ once at two different time slices [$N_\tau(N_\tau - 1)/2$ terms]. Both of these kinds of terms are $O(\tau^2)$, but the first kind scale only as N_τ and will therefore drop out at large N_τ (i.e., in the small τ limit, holding β fixed). (Another way of saying this is that the diagonal terms will form a set of measure zero in the continuum limit.) Thus, the result for $n = 2$ is

$$e^{-\beta\hat{D}} \sum_{k_2=1}^{N_\tau} \sum_{k_1=1}^{k_2-1} e^{\tau k_2\hat{D}}(-\tau\hat{K})e^{-\tau(k_2-k_1)\hat{D}}(-\tau\hat{K})e^{-\tau k_1\hat{D}}. \quad \text{(A4)}$$

Proceeding in this fashion order by order in n, and summing over n from 0 to ∞, we obtain Eq. (12) in the main text.

For the second approach, we seek an expression for the evolution operator

$$\hat{U}(\beta) = e^{-\beta(\hat{D}+\hat{K})} = e^{-\beta\hat{D}}\hat{O}(\beta), \quad \text{(A5)}$$

where we have defined the imaginary-time-dependent operator

$$\hat{O}(\tau) \equiv e^{\tau\hat{D}}e^{-\tau(\hat{D}+\hat{K})}, \quad \text{(A6)}$$

whose time derivative is

$$-\frac{\partial\hat{O}(\tau)}{\partial\tau} = \hat{K}_I(\tau)\hat{O}(\tau), \quad \text{(A7)}$$

where

$$\hat{K}_I(\tau) \equiv e^{\tau\hat{D}}\hat{K}e^{-\tau\hat{D}}. \quad \text{(A8)}$$

Integrating Eq. (A7) with $\hat{O}(0) = \mathbb{1}$ as the initial condition, we arrive at the integral equation

$$\hat{O}(\beta) = \mathbb{1} + \int_0^\beta d\tau\, \frac{\partial\hat{O}(\tau)}{\partial\tau} = \mathbb{1} - \int_0^\beta d\tau \hat{K}_I(\tau)\hat{O}(\tau). \quad \text{(A9)}$$

Iteratively substituting Eq. (A9) into itself generates a Dyson series,

$$\hat{O}(\beta) = \Bigg[\mathbb{1} - \int_0^\beta d\tau_1\, \hat{K}_I(\tau_1) + \int_0^\beta d\tau_1 \int_0^{\tau_1} d\tau_2\, \hat{K}_I(\tau_1)\hat{K}_I(\tau_2) - \cdots\Bigg]. \quad \text{(A10)}$$

To evaluate the partition function $\mathcal{Z} = \mathrm{Tr}[e^{-\beta(\hat{D}+\hat{K})}]$, then, it suffices to evaluate the trace of $\hat{U}(\beta)$ using the above expression for $\hat{O}(\beta)$. Doing that and expanding the $\hat{K}_I$ terms

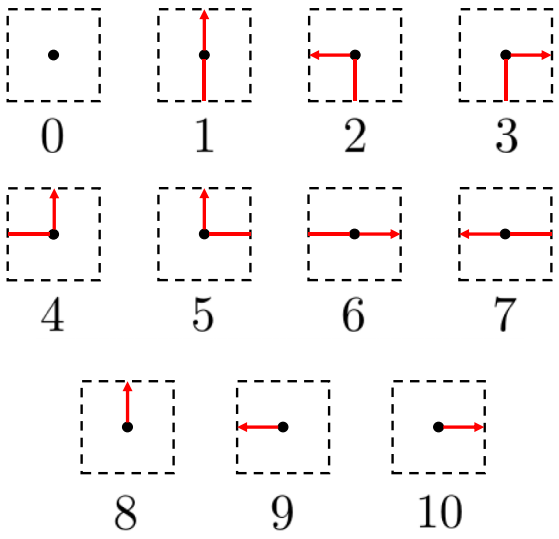

FIG. 11. Local configurations of worldlines, with labels corresponding to those used in Table I. Note that each lattice site is associated with two segments of the worldline, each with their own weight. To avoid double-counting, we follow Ref. [43] and by convention associate the weight of a lattice site with the *outgoing* segment of the worldline (indicated by the arrowheads).

TABLE I. Map of all possible local lattice updates in the worm algorithm, where integer labels correspond to those in Fig. 11. The outgoing directions are each respective to the possible final states.

Initial state	Incoming worm direction	Possible final states	Outgoing worm direction
0	Up	0, 1, 2, 3	Down, up, left, right
	Left	0, 5, 7	Right, up, left
	Right	0, 4, 6	Left, up, right
1	Down	0, 1, 2, 3	Down, up, left, right
	Left	5	Down
	Right	4	Down
2	Right	0, 1, 2, 3	Down, up, left, right
	Left	7	Down
3	Left	0, 1, 2, 3	Down, up, left, right
	Right	6	Down
4	Down	0, 4, 6	Left, up, right
	Up	1	Left
	Left	5	Left
5	Down	0, 5, 7	Right, up, left
	Up	1	Right
	Right	4	Right
6	Left	0, 4, 6	Left, up, right
	Up	3	Left
7	Right	0, 5, 7	Right, up, left
	Up	2	Right
8	Up	1	Update complete
	Right	4	
	Left	5	
	Down	0	
9	Up	2	Update complete
	Left	7	
	Right	0	
10	Up	3	Update complete
	Right	6	
	Left	0	

using Eq. (A8), we obtain

$$\mathcal{Z} = \sum_{k=0}^{\infty} \int_0^{\beta} d\tau_k \int_0^{\tau_k} d\tau_{k-1} \ldots \times \int_0^{\tau_2} d\tau_1 \, \mathrm{Tr}[e^{-(\beta-\tau_k)\hat{D}} \hat{K} e^{-(\tau_k-\tau_{k-1})\hat{D}} \hat{K} \ldots \hat{K} e^{-\tau_1 \hat{D}}], \tag{A11}$$

which yields Eq. (12) upon discretization.

APPENDIX B: MAP OF LOCAL UPDATES

Accounting forall possible worldline moves, any lattice site can be represented as one of a finite set of allowed configurations. In Fig. 11, the complete set of such configurations is depicted. The tiles of the top two rows correspond to physical configurations; those of the bottom row exist only as intermediate steps in the updating algorithm and are never present during a measurement of observables. All possible transitions between these local configurations, defining the paths the worm is allowed to follow, are collected in Table I.

In Table I, the incoming and outgoing worm directions are best illustrated by examples. With an initial state labeled by 0, an incoming worm direction of "up" means that the worm has entered via the site immediately "below" the present one in imaginary time (see Fig. 2). The possible final states are then those labeled by either 1, 2, or 3. The outgoing worm directions would then be up, left, and right, respectively—precisely the directions indicated by the arrowheads. Whichever of these directions is selected then becomes the "incoming" direction of the next site visited. In this example, a final state labeled by 0 is also possible but would constitute a "bounce," where the worm reverses direction in imaginary time. The outgoing worm direction would thus be down (opposite the direction of entry), as would the incoming worm direction of the lattice site immediately "below" the initial site (which becomes the new "initial" state).

Excluding the bounce, the previous example showed the worm traversing the lattice in the forward direction of imaginary time, so that its motions were parallel to the arrowheads in Fig. 11. As indicated by the bounce, however, the worm can also move backwards in imaginary time (antiparallel to the arrowheads). In such cases, the "incoming" direction is *always* antiparallel to the arrowhead, reflecting the fact that

intersections of worldlines only occur while the worm is moving forwards in imaginary time. The entries of Table I provide a complete prescription for automatically handling the possible transitions for a given initial state and incoming direction, regardless of whether the worm is moving forwards or backwards in imaginary time.

APPENDIX C: CONTACT FROM THE ANOMALY IN THE EQUATION OF STATE AND LATTICE EFFECTS

In a d-dimensional nonrelativistic scale-invariant system, dimensional arguments dictate that the pressure must take the form

$$P = \beta^{\alpha} f(\beta\mu), \tag{C1}$$

where $\alpha = -(d+2)/2$. Using the thermodynamic identities

$$-PV = E - TS - \mu N, \tag{C2}$$

$$S = V\frac{\partial P}{\partial T}, \tag{C3}$$

$$N = V\frac{\partial P}{\partial \mu}, \tag{C4}$$

where $V = L^d$, it is straightforward to see that

$$-PV = E + V\beta^{\alpha}\alpha f(\beta\mu) = E + \alpha PV, \tag{C5}$$

such that

$$P + \frac{1}{\alpha+1}\frac{E}{L^d} = 0, \tag{C6}$$

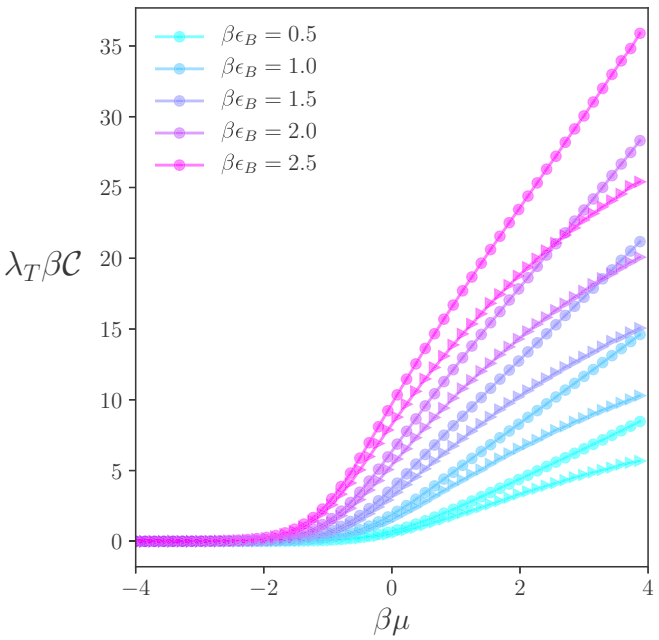

FIG. 12. Contact density for lattice size $N_x = 80$ as obtained from the pressure-energy relation compared to the contact obtained from Eq. (34). For each coupling, the former is shown with triangles and the latter with circles. The coupling strength $\beta\epsilon_B$ in each pair of data sets increases from bottom to top.

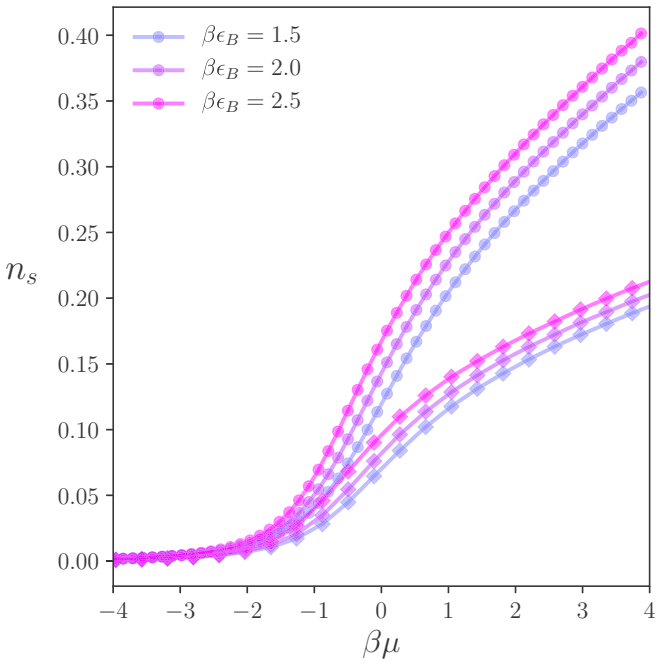

FIG. 13. Density per species n_s in lattice units, as a function of $\beta\mu$. The solid lines interpolate our Monte Carlo results shown with symbols. Circles show the data for $N_x = 80$, and diamonds correspond to $N_x = 140$. As expected the latter are considerably lower than the former, which should facilitate the approach to the continuum limit. In both data sets, the coupling increases from the bottom curves to the top curves.

where $1/(\alpha+1) = -2/d$ and we used $V = L^d$. Thus, in 1D, a nonrelativistic scale-invariant system obeys

$$P - 2E/L = 0. \tag{C7}$$

When scale or nonrelativistic invariance are broken, the above pressure-energy (P-E) relation is modified. For example, for the noninteracting case in a box, the relationship becomes $P - \frac{1}{\beta E_1}\frac{E}{L} = 0$, where E_1 is the average energy of a single particle at finite inverse temperature β:

$$E_1 = \frac{1}{Q_1}\sum_k \epsilon_k e^{-\beta\epsilon_k}, \tag{C8}$$

where Q_1 is the single-particle partition function. In the large-box limit, $1/\beta E_1 \to 2$, and the expected P-E relation Eq. (C7) is recovered.

When scale invariance is broken by interactions, as in our case, a nonvanishing contribution appears on the right-hand side of the P-E relation Eq. (C6), namely the contact density $\mathcal{C}$, as mentioned in the main text. We have calculated the left-hand side and show it in Fig. 12 compared with the right-hand side, namely the contact as calculated in the main text Eq. (34). For $\beta\mu$ up to roughly $\beta\mu \simeq 0$, the results track each other closely. Differences start to appear beyond that point and increase as $\beta\mu$ increases, leading to differences of up to 25%, likely due to lattice spacing effects which break nonrelativistic invariance (the finite-box effect described above was already accounted for in this plot). If the latter were restored, both approaches would yield the same result. In order to restore the

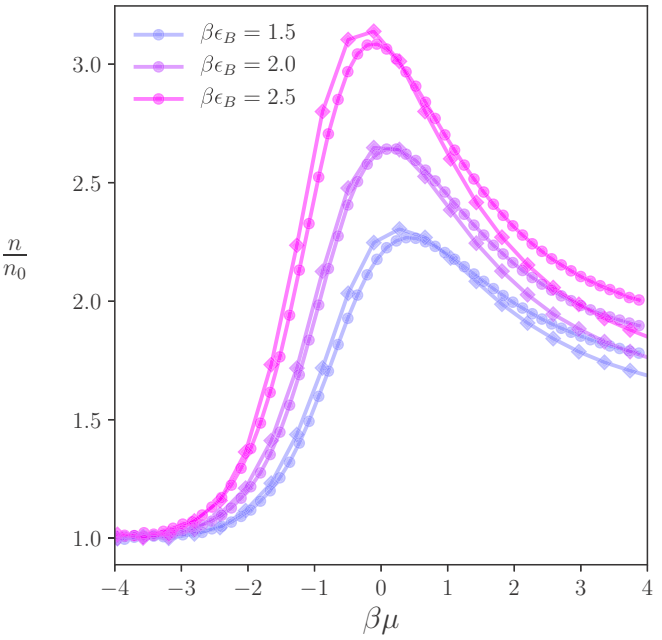

FIG. 14. The density n in units of the noninteracting density n_0 as a function of the dimensionless parameter $\beta\mu$ and the coupling strength $\beta\epsilon_B$ (increasing from bottom data sets to top data sets). The solid lines interpolate our Monte Carlo results shown with symbols. Circles show the data for $N_x = 80$, and diamonds correspond to $N_x = 140$.

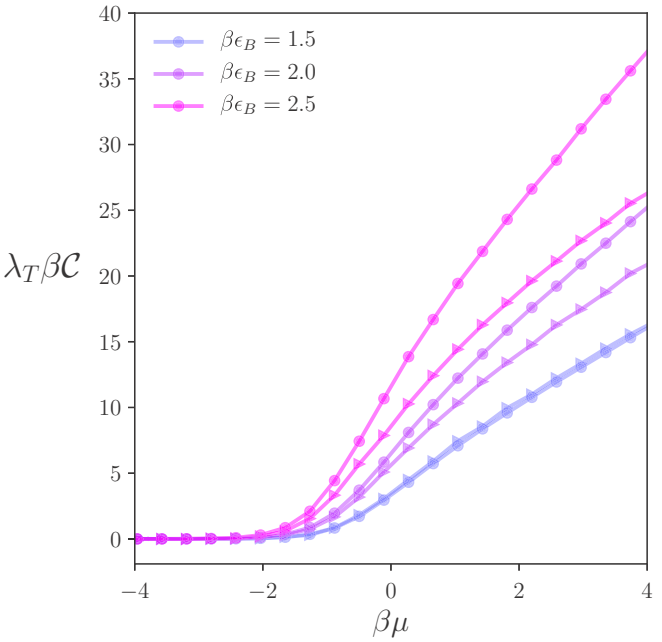

FIG. 15. Contact density for lattice size $N_x = 140$ as obtained from the pressure-energy relation compared to the contact obtained from Eq. (34). For each coupling (increasing from bottom to top), the latter (circles) yields larger values than the former (triangles). Comparing with Fig. 12, which shows the same quantity for a smaller lattice size $N_x = 80$, the two ways of computing the contact are here in better agreement at weaker couplings, but remain large (essentially unchanged from $N_x = 80$) for the strongest coupling.

symmetries at increased densities, improved operators would need to be used (see, e.g., Ref. [52]). Unfortunately, such improved operators involve nonlocal kinetic-energy terms which will result in a sign problem and are therefore beyond the scope of this work.

To display more precisely the lattice effects, we show in Fig. 13 the density per species n_s in lattice units (i.e., the lattice filling per species) for $N_x = 80$ (main text) and $N_x = 140$ (for comparison). As the latter yield lower lattice densities when all the physical parameters are kept constant, i.e., the lattice theory is more dilute, it is expected that the continuum limit is better approximated [cf. Eq. (19)]. Figure 14 displays such effects for the density equation of state n/n_0, for the same parameter values as those of Fig. 13. As expected, the effects are especially large at the highest lattice densities (i.e., largest values of $\beta\mu$) and increase as $\beta\epsilon_B$ is increased. Similarly, Fig. 15 shows the contact compared in two different ways, as in Fig. 12. Here as well, lattice effects are large at high density (i.e., largest values of $\beta\mu$) and increase as $\beta\epsilon_B$ is increased. However, better agreement between the two ways to calculate the contact is found at the weakest coupling explored for this comparison. Based on the above, we conclude that, while lattice effects are certainly present in our calculations, especially at the highest densities and strongest couplings, they do not represent a qualitative modification of the data shown in the main text. We leave further exploration of lattice artifacts and an improved approach to the continuum limit (particularly for strong couplings) to future work.

[1] Y. Sekino and Y. Nishida, Phys. Rev. A **97**, 011602(R) (2018).
[2] Y. Nishida, Phys. Rev. A **97**, 061603(R) (2018).
[3] L. Pricoupenko, Phys. Rev. A **97**, 061604(R) (2018).
[4] G. Guijarro, A. Pricoupenko, G. E. Astrakharchik, J. Boronat, and D. S. Petrov, Phys. Rev. A **97**, 061605(R) (2018).
[5] J. E. Drut, J. R. McKenney, W. S. Daza, C. L. Lin, and C. R. Ordóñez, Phys. Rev. Lett. **120**, 243002 (2018).
[6] J. R. McKenney and J. E. Drut, Phys. Rev. A **99**, 013615 (2019).
[7] M. Valiente and V. Pastukhov, Phys. Rev. A **99**, 053607 (2019).
[8] M. Valiente, Phys. Rev. A **100**, 013614 (2019).
[9] J. Maki and C. R. Ordóñez, Phys. Rev. A **100**, 063604 (2019).
[10] A. Pricoupenko and D. S. Petrov, Phys. Rev. A **100**, 042707 (2019).
[11] A. J. Czejdo, J. E. Drut, Y. Hou, J. R. McKenney, and K. J. Morrell, Phys. Rev. A **101**, 063630 (2020).
[12] R. Jackiw, in *M.A.B. Beg Memorial Volume*, edited by A. Ali and P. Hoodbhoy (World Scientific, Singapore, 1991), pp. 1–16.
[13] B. R. Holstein, Am. J. Phys. **61**, 142 (1993).
[14] L. P. Pitaevskii and A. Rosch, Phys. Rev. A **55**, R853 (1997).
[15] C. Chafin and T. Schäfer, Phys. Rev. A **88**, 043636 (2013).
[16] C. R. Ordonez, Physica A (Amsterdam, Neth.) **446**, 64 (2016).
[17] W. Daza, J. E. Drut, C. Lin, and C. Ordóñez, Phys. Rev. A **97**, 033630 (2018).

[18] F. Werner and Y. Castin, Phys. Rev. A **86**, 013626 (2012).
[19] J. Hofmann, Phys. Rev. Lett. **108**, 185303 (2012).
[20] E. Taylor and M. Randeria, Phys. Rev. Lett. **109**, 135301 (2012).
[21] S. Tan, Ann. Phys. **323**, 2952 (2008).
[22] S. Tan, Ann. Phys. **323**, 2971 (2008).
[23] S. Tan, Ann. Phys. **323**, 2987 (2008).
[24] K. Martiyanov, V. Makhalov, and A. Turlapov, Phys. Rev. Lett. **105**, 030404 (2010).
[25] B. Fröhlich, M. Feld, E. Vogt, M. Koschorreck, W. Zwerger, and M. Köhl, Phys. Rev. Lett. **106**, 105301 (2011).
[26] Y. Zhang, W. Ong, I. Arakelyan, and J. E. Thomas, Phys. Rev. Lett. **108**, 235302 (2012).
[27] A. A. Orel, P. Dyke, M. Delehaye, C. J. Vale, and H. Hu, New J. Phys. **13**, 113032 (2011).
[28] E. Vogt, M. Feld, B. Fröhlich, D. Pertot, M. Koschorreck, and M. Köhl, Phys. Rev. Lett. **108**, 070404 (2012).
[29] B. Fröhlich, M. Feld, E. Vogt, M. Koschorreck, M. Köhl, C. Berthod, and T. Giamarchi, Phys. Rev. Lett. **109**, 130403 (2012).
[30] V. Makhalov, K. Martiyanov, and A. Turlapov, Phys. Rev. Lett. **112**, 045301 (2014).
[31] W. Ong, C. Cheng, I. Arakelyan, and J. E. Thomas, Phys. Rev. Lett. **114**, 110403 (2015).
[32] M. G. Ries, A. N. Wenz, G. Zürn, L. Bayha, I. Boettcher, D. Kedar, P. A. Murthy, M. Neidig, T. Lompe, and S. Jochim, Phys. Rev. Lett. **114**, 230401 (2015).
[33] P. A. Murthy, I. Boettcher, L. Bayha, M. Holzmann, D. Kedar, M. Neidig, M. G. Ries, A. N. Wenz, G. Zürn, and S. Jochim, Phys. Rev. Lett. **115**, 010401 (2015).
[34] K. Fenech, P. Dyke, T. Peppler, M. G. Lingham, S. Hoinka, H. Hu, and C. J. Vale, Phys. Rev. Lett. **116**, 045302 (2016).
[35] G. Bertaina and S. Giorgini, Phys. Rev. Lett. **106**, 110403 (2011).
[36] H. Shi, S. Chiesa, and S. Zhang, Phys. Rev. A **92**, 033603 (2015).
[37] E. R. Anderson and J. E. Drut, Phys. Rev. Lett. **115**, 115301 (2015).
[38] L. Rammelmüller, W. J. Porter, and J. E. Drut, Phys. Rev. A **93**, 033639 (2016).
[39] J. Levinsen and M. M. Parish, in *Annual Review of Cold Atoms and Molecules* (World Scientific, Singapore, 2015), Vol. 3, pp. 1–75.
[40] U. Schollwöck, Rev. Mod. Phys. **77**, 259 (2005).
[41] J. von Delft and H. Schoeller, Ann. Phys. **7**, 225 (1998).
[42] X.-W. Guan, M. T. Batchelor, and C. Lee, Rev. Mod. Phys. **85**, 1633 (2013).
[43] H. Singh and S. Chandrasekharan, Phys. Rev. D **99**, 074511 (2019).
[44] M. G. Endres, Phys. Rev. A **85**, 063624 (2012).
[45] Y. Nishida and D. T. Son, Phys. Rev. A **82**, 043606 (2010).
[46] M. G. Endres, Phys. Rev. Lett. **109**, 250403 (2012).
[47] M. G. Endres, Phys. Rev. A **87**, 063617 (2013).
[48] A. Goban, R. Hutson, G. Marti, S. Campbell, M. Perlin, P. Julienne, J. D'Incao, A. Rey, and J. Ye, Nature (London) **563**, 369 (2018).
[49] L. A. Reynolds, E. Schwartz, U. Ebling, M. Weyland, J. Brand, and M. F. Andersen, Phys. Rev. Lett. **124**, 073401 (2020).
[50] M. D. Hoffman, P. D. Javernick, A. C. Loheac, W. J. Porter, E. R. Anderson, and J. E. Drut, Phys. Rev. A **91**, 033618 (2015).
[51] M. Girardeau, J. Math. Phys. **1**, 516 (1960).
[52] J. E. Drut, Phys. Rev. A **86**, 013604 (2012).